

Article

Dehydrogenation Catalysts for Synthesis of O-Phenylphenol via Cu/Ni/Mg/Al Hydrotalcite-Like Compounds as Precursors

Jilong Wang ¹, Tianchi Zhang ^{1,2}, Kai Li ¹, Yanan Cao ¹ and Yongping Zeng ^{1,*} 

¹ College of Chemistry and Chemical Engineering, Yangzhou University, Yangzhou 225002, China; wangjilong7559135@gmail.com (J.W.); tianchi.zhang.1@ulaval.ca (T.Z.); kai30869@gmail.com (K.L.); caoyanan96@gmail.com (Y.C.)

² Département de Chimie, Université Laval, Québec, QC G1K 7P4, Canada

* Correspondence: ypzeng@yzu.edu.cn; Tel.: +86-514-8797-5590 (ext. 9109)

Received: 19 February 2018; Accepted: 28 April 2018; Published: 2 May 2018



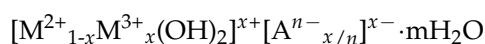
Abstract: A series of copper containing catalysts were prepared by calcination of Cu/Ni/Mg/Al hydrotalcite-like precursors, using the coprecipitation method. The materials were characterized and show a well-crystallized layered structure of hydrotalcite with smaller Cu⁰ particles. We also studied their catalytic performance for conversion of 2-(1-cyclohexenyl) cyclohexanone into o-phenylphenol. The catalysts containing Ni showed higher catalytic activity; the optimum stability occurred when the Ni²⁺:(Ni²⁺ + Cu²⁺) atomic ratio was 0.4. The combination of Cu and Ni can greatly improve the stability and activities of the catalyst.

Keywords: dehydrogenation; Cu/Ni/Mg/Al; hydrotalcite; ortho-phenylphenol

1. Introduction

O-phenylphenol (OPP) is an important chemical product and is widely used as a heat stability solvent, medicine, dyeing auxiliary, biocide, etc. [1,2]. Because of the extensive application of OPP in various fields, its demand is increasing [3]. OPP is industrially produced, mainly by catalytic dehydrogenation of 2-(1-cyclohexenyl) cyclohexanone (CHCH) over a noble metal-based catalyst, such as Pt, Pd, Ru, etc. [4–6]. Though showing good activity, the cost of using these catalysts in industrial processes is high. The catalytic performance of non-noble metals has been reported in the literature [7,8].

Layered double hydroxides (LDH) combine the positively charged laminate and negatively charged interlayer anions with the empirical formula [8]:



where M²⁺ and M³⁺ are divalent and trivalent metal cations, Aⁿ⁻ is the anion of the interlayer, and x refers to the ratio of M³⁺/(M²⁺ + M³⁺). The divalent metal cations are generally Mg²⁺, Ni²⁺, Cu²⁺, etc. M³⁺ trivalent metal ions are mainly Al³⁺, Cr³⁺, Fe³⁺, etc. However, Cu²⁺ does not enter easily into the brucite-like layers due to its pronounced Jahn–Teller effect, except for the case when another divalent cation is present in the solution [8]. The interlayer anions are mainly CO₃²⁻, Cl⁻, NO₃³⁻, SO₄²⁻, OH⁻, etc.

Cu/Mg/Al catalysts have been applied in various reactions [9–11]. Zhou et al. reported the superior activity of Cu/Al/Mg catalysts for the selective oxidation of biorenewable glycerol, in which Cu⁰ was taken as an active center [12]. Previous studies in our group have also shown that catalysts with Cu⁰ as their active center exhibit strong activity for the dehydrogenation of 2-(1-cyclohexenyl)

cyclohexanone to OPP [3]. OPP has a selectivity of up to 90%. However, the selectivity of the catalysts decreased by 87% after the 3 h reaction; at the same time, the activity of the catalysts declined rapidly. Some research articles have shown that these catalysts have higher stability in the presence of Ni [13,14]. Alejandre et al. used copper–nickel catalysts to oxidize an aqueous solution of phenol and showed that the yield of the target compound and the crystallinity of the hydrotalcite sample of the Ni containing catalyst were higher than the sample that did not contain Ni [15]. Mariño et al. introduced Ni into Cu-based hydrotalcite, and found that it could enhance the stability for the ethanol steam reforming reaction over calcined hydrotalcite catalysts [16]. Therefore, the goal of this work is to design a high stability and selective copper–nickel catalytic material for the conversion of 2-(1-cyclohexenyl) cyclohexanone to OPP. Ni was introduced to the Cu-based hydrotalcite-like catalysts with different Cu/Ni/Mg/Al ratios. The catalysts with Cu⁰ as their active sites were obtained by H₂ reduction after calcination of hydrotalcite precursors. The effect of Ni content on the stability and activity of the catalysts was investigated.

2. Results and Discussions

2.1. Characterization of Structural Properties

Figure 1 shows the XRD patterns of the hydrotalcite-like precursor and the reduced samples with H₂ for 2 h. As shown in Figure 1a, an obvious multicationic hydrotalcite structure can be observed with a sharpness of (003), (006), (009), (015), (018), (110), and (113), the reflections indicated that the samples were crystalline LDH. This observation was in agreement with the literature [17–21]. It can be inferred that the introduction of Ni did not cause the damage to the hydrotalcite structure (JCPDS 48-0601). In addition, no other oxides or hydroxides were detected in Figure 1a, indicating that all metal ions were evenly distributed in the layered structure. Figure 1b shows that the XRD patterns of the samples calcined after reduction by H₂. As can be observed by XRD, there are no characteristic peaks of hydrotalcite-like compounds. In addition, the crystalline phase of Ni was not detected in CNMA-(0-4). However, the crystalline phase was found in the XRD pattern for the Ni/Mg/Al catalyst when calcined. This can be ascribed to the higher reducibility of Cu compared to Ni (this will be discussed in H₂-TPR). Thus, Ni²⁺ can hardly be reduced at this temperature. These results may be due to a failure to reach the reduction temperature of Ni. De Bokx et al. have reported that Ni²⁺ can only be reduced to metal Ni above a temperature of 450 °C [22,23]. CNMA-(0-4) contained only one peak characteristic of the copper phase; this is because of the relative contents of the different metal cations and calcination temperature. Identification of metal species in the surface of reduced CNMA-4 was characterized by X-ray photoelectron spectroscopy (XPS). As shown in Figure 2, the peak of C 1s was attributed to the adventitious hydrocarbon from the XPS apparatus. The reduced CNMA-4 shows signatures of Cu⁰/Cu⁺ with binding energies of 932.3 eV and 952.4 eV, which correspond to the peaks of Cu 2p_{3/2} and Cu 2p_{1/2}, respectively. These peaks were assigned to Cu⁰/Cu⁺ from Cu⁰/Cu₂O. The binding energies of 933.8 eV and 953.7 eV corresponded to Cu²⁺ 2p_{3/2} and Cu²⁺ 2p_{1/2}, respectively, which were attributed to Cu²⁺ from CuO. The associated satellite peak was observed at ~942.4 eV. When the reduced CNMA-4 was transferred to the XPS chamber, the exposed air may have caused the oxidation of partial Cu⁰. The Ni 2p spectra were observed at 855.6 eV and 873.0 eV, which is consistent with the binding energy peak of Ni 2p_{3/2} and Ni 2p_{1/2}, respectively. These peaks were assigned to Ni²⁺ from NiO, and the satellite peaks were observed at 861.3 eV and 865.1 eV. The Al 2p spectrum shows the signature of Al³⁺ with binding energies of 74.0 eV, corresponding to Al₂O₃. The results of the XPS analyses were in agreement with the XRD results. The other metal oxides, except for the copper oxides, can also be found in the spectra, but not found in the XRD pattern, probably due to the high dispersion of the catalysts.

To understand the effect of the Cu/Ni ratio on the size of Cu⁰ particles, we showed the full width at half maximum (FWHM) and the size of copper particles in the XRD pattern in Table S1. We found that the average size of Cu⁰ was between 3.5 nm and 5.5 nm after H₂ reduction. With an increase in

the Ni content, the size of the copper particles decreased gradually [22]; CNMA-4 reached a minimum average size of 3.5 nm. This indicates that Ni content has a significant effect on the size of Cu^0 particles.

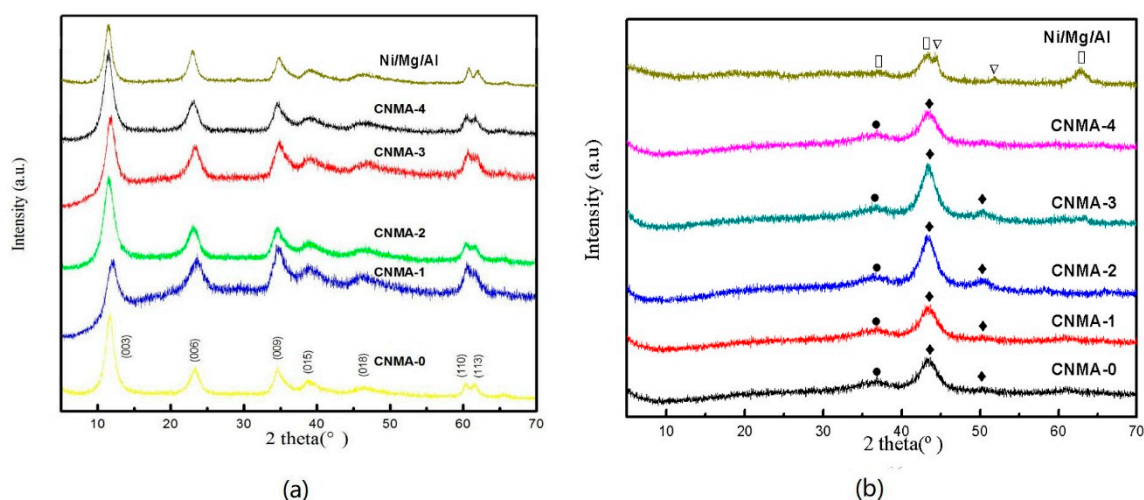


Figure 1. XRD of the Cu/Ni/Mg/Al precursors. (a) Calcined Cu/Ni/Mg/Al catalysts after being reduced at 300 °C; (b) (●) Cu_2O ; (◆) Cu^0 ; (□) NiO; (▽) Ni.

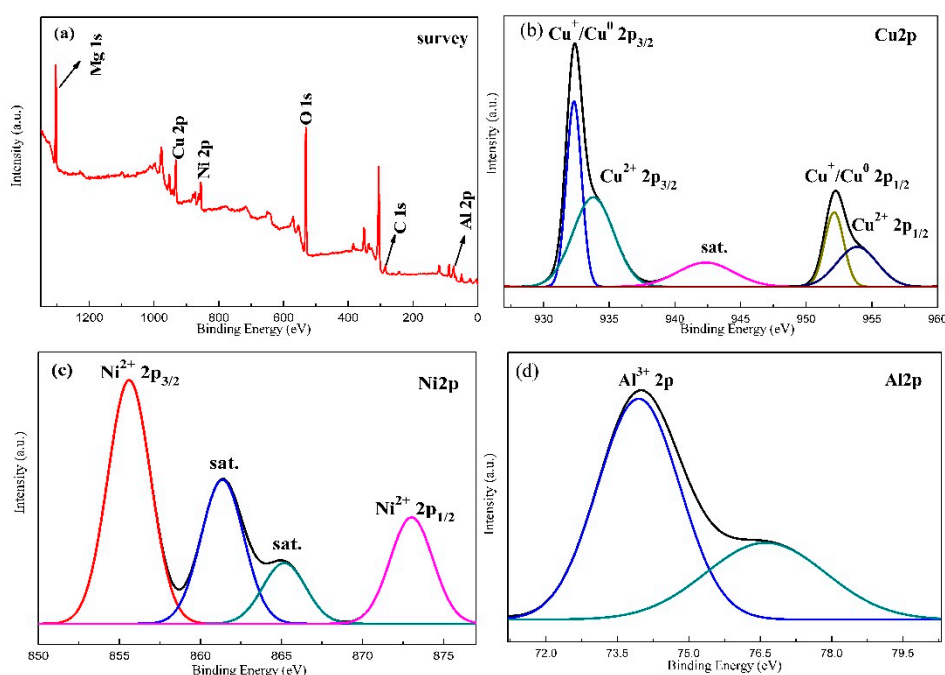


Figure 2. X-ray photoelectron spectroscopy (XPS) spectra of the reduced CNMA-4: (a) survey; (b) Cu2p; (c) Ni2p; and (d) Al2p.

The SEM results of all the hydrotalcite-like compounds are shown in Figure 3. All the samples were present in the layered structure. The layered structure of hydrotalcite for CNMA-(1~4) containing Ni was more orderly when compared with CNMA-0 without adding Ni. Similar observations have been documented in the literature [8,24,25]. When the ratio of Cu/Ni reaches 1.25/0.25, CNMA-1 forms a regular staggered lamellar structure. In addition, the introduction of nickel reduces the thickness of the hydrotalcite laminates. The thickness of the CNMA-0 laminates is greater than 30 nm, while that of CNMA-2 drops to around 15–20 nm. It shows that the introduction of an appropriate amount of Ni can result in a thinner layer of hydrotalcite.

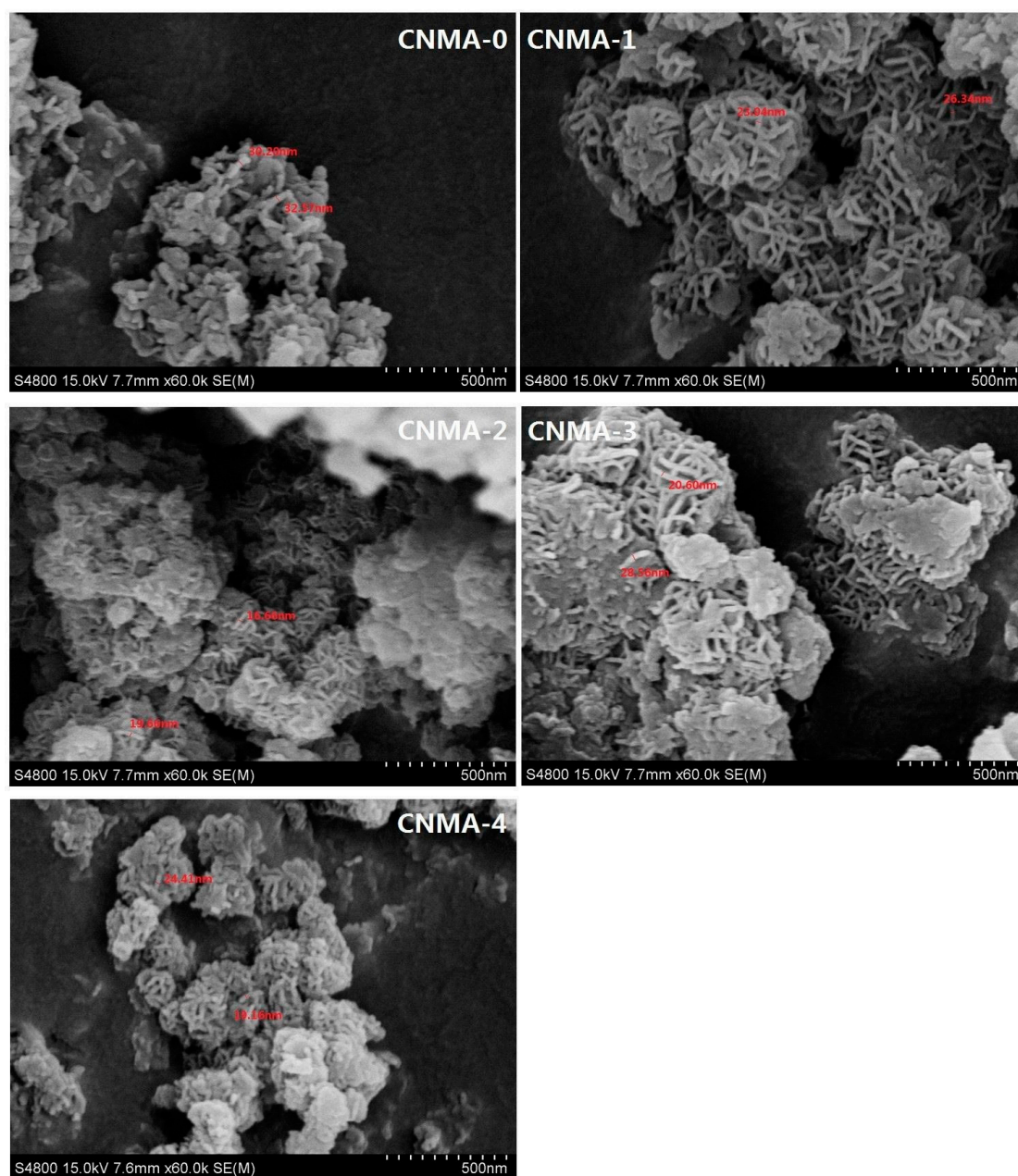


Figure 3. SEM of the hydrotalcite-like precursors with different ratios of Cu:Ni:Mg:Al.

The FT-IR spectra of the precursors and calcined samples are shown in Figure S1. The vibration peaks at 3500 cm^{-1} are attributed to water molecules between the layers and the hydroxyl groups on the laminates. The weak absorption peak at 1600 cm^{-1} is due to the distortion of H_2O molecules [26]. The peaks at 1300 cm^{-1} and 1550 cm^{-1} are ascribed to the stretching vibration of the carbonate between the layers. Also, at 1000 cm^{-1} to 500 cm^{-1} , there are a series of stretching vibration peaks, which are ascribed to the vibrations of the O–metal–O bond. Figure S1 also confirmed that the hydrotalcite structure was still observed when introducing Ni, which is in agreement with the XRD results. After calcination, the peak at 3500 cm^{-1} was obviously weakened, as shown in Figure S1b, as the water molecules and the hydroxyl groups on the laminates had decomposed. Meanwhile, the CO_3^{2-} stretching vibration at 1380 cm^{-1} of the interlayers was also significantly reduced [27]. The intensity of the vibration peak at 1000 cm^{-1} to 500 cm^{-1} (ascribed to the vibrations of the O–metal–O bond) decreased, indicating the damaged hydrotalcite plates.

To clarify the decomposition process of the precursors, the thermophysical properties were studied by TG and DTG and the results are shown in Figure S2. There are three major loss stages: The mass loss corresponding to the peak at 100–150 °C is due to the loss of physically adsorbed water, the second mass loss phase occurs at the range of 250–400 °C, which is due to the decomposition of carbonates and the dehydration of hydroxyl groups between laminates, the third endothermic peak appears in the range of 600–650 °C, which is due to the decomposition of the layered structure.

Nitrogen adsorption–desorption isotherms of reduced catalysts are shown in Figure S3. The two samples were presented with IV type isotherms based on the IUPAC classification corresponding to their mesoporous features. The specific surface area, pore volume, and average pore size of the samples is shown in Table S2. The adsorption curves in the low relative pressure region show that the catalysts have a small number of micropores for CNMA-(0~4). Additionally, the volume of micropores increases with increasing nickel content in the catalysts. A narrow hysteresis loop occurs at a relative pressure of 0.4, due to the capillary condensation of the mesoporous structure of the catalyst. This indicated that the hydrotalcite structure disappeared and the slit-type channels formed after the calcination at high-temperature [28]. Figure S4 shows a bimodal pore size distribution between 3.3 and 100 nm. As shown in Table S2, the specific surface area of the samples ranged from 37 to 144 m²·g⁻¹. The pore volume and specific surface area of the samples was enhanced by the introduction of Ni, which is plausible because Ni reduces the thickness of the laminate and degrades the ameliorates of the LDH regularity (confirmed by SEM).

Figure 4 shows a TEM image of the Cu⁰ particles (left) and corresponding size distribution (right) of the reduced CNMA-(0~4) with different Cu/Ni ratios. The size of Cu particles was measured by 100 particles. As shown in Figure 4, metallic copper particles of CNMA-(0~4) are homogeneously distributed on a relatively narrow size distribution. With an increase in the percentage of Ni, the copper particle size decreased, which shows that Ni can regulate the size of Cu⁰ particles in the catalysts. To further investigate the structure of copper nanoparticles in the oxide matrix, an image taken with HRTEM is shown in Figure 5. Figure 5b shows the fringe space of 1.21 Å, which illustrates the presence of Cu⁰ particles (110) [29]. Figure S5 shows the HRTEM elemental mapping images of CNMA-4 and elemental mapping showing a homogeneous distribution of all the elements in the oxide matrix.

2.2. H₂-TPR

H₂-TPR images of the calcined sample are shown in Figure 6. We can observe that the reduction peak for all samples is in the range of 150–450 °C. In order to obtain more information, the H₂ consumption band is deconvoluted into three Gaussian forms, assigned as α , β , and γ peaks. The reduction temperatures corresponding to the peaks were shown in Table S3. The three types of peaks were due to the different morphology of CuO, where α peaks are owing to the high dispersibility of CuO, the β peak is attributed to the moderate dispersibility of CuO, and the γ peak is due to the poor dispersion of CuO [30]. As shown in Table S3, the ratio of the α peak of CNMA-0 is only 12.07%. The α peak of CNMA-2 increases with the amount of Ni, and approaches the maximum. The proportion of Ni in the catalyst has a significant effect on the reduction of CuO [31]. It is remarkable that the reduction peak of CNMA-(2-4) was shifted at higher temperature. For the CNMA-(2-4) catalysts, we observe a peak at 390 °C, probably owing to a strong interaction between Cu and Ni [32,33]. Contrastingly, the reduction peak had shifted to lower temperature for CNMA-1 with low Ni content. It indicated that a little amount of nickel could significantly promote the reduction of metal oxides, which also was observed by Shi et al. [34].

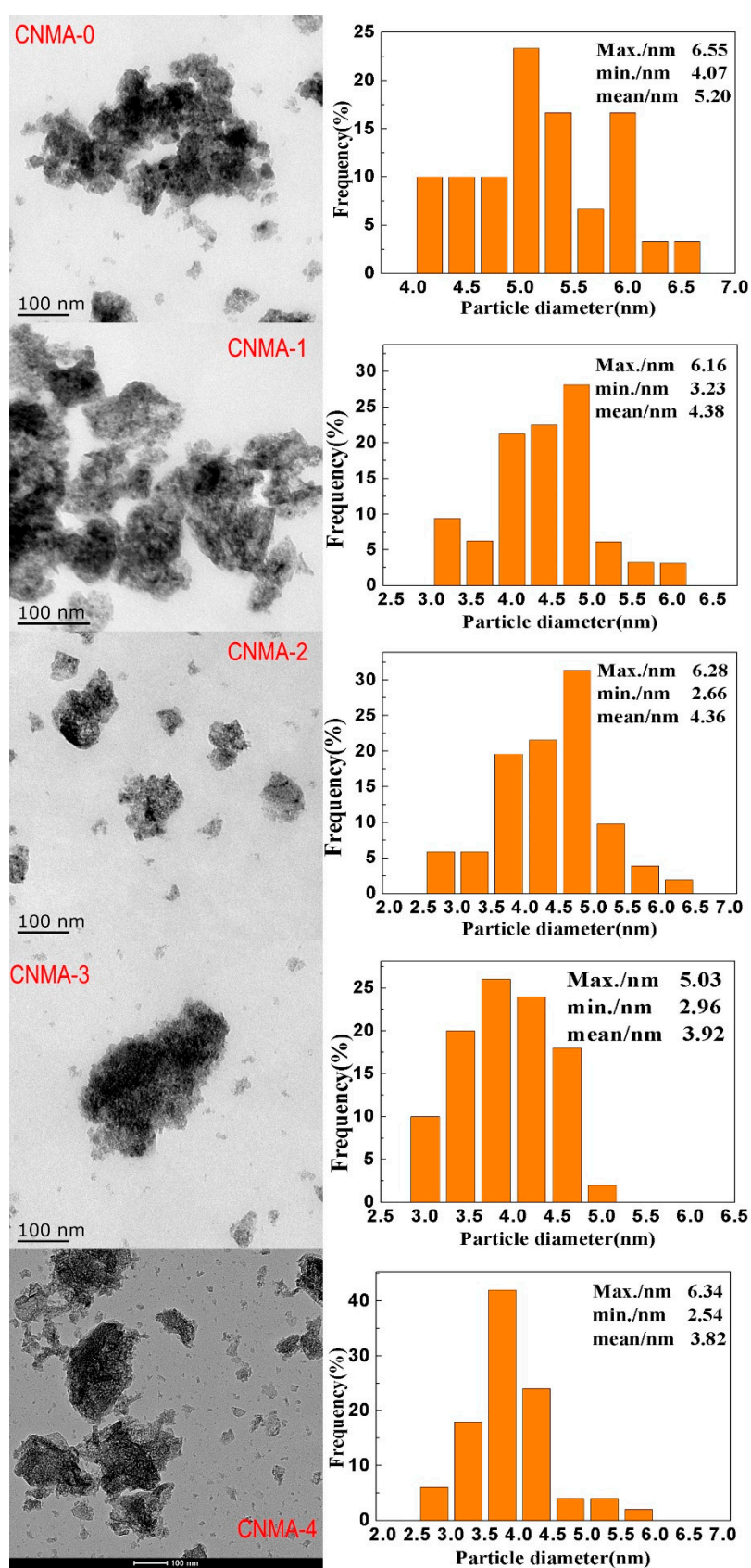


Figure 4. TEM images (left) and corresponding Cu particle size distribution (right) of the catalysts reduced with H₂ at 300 °C for 2 h.

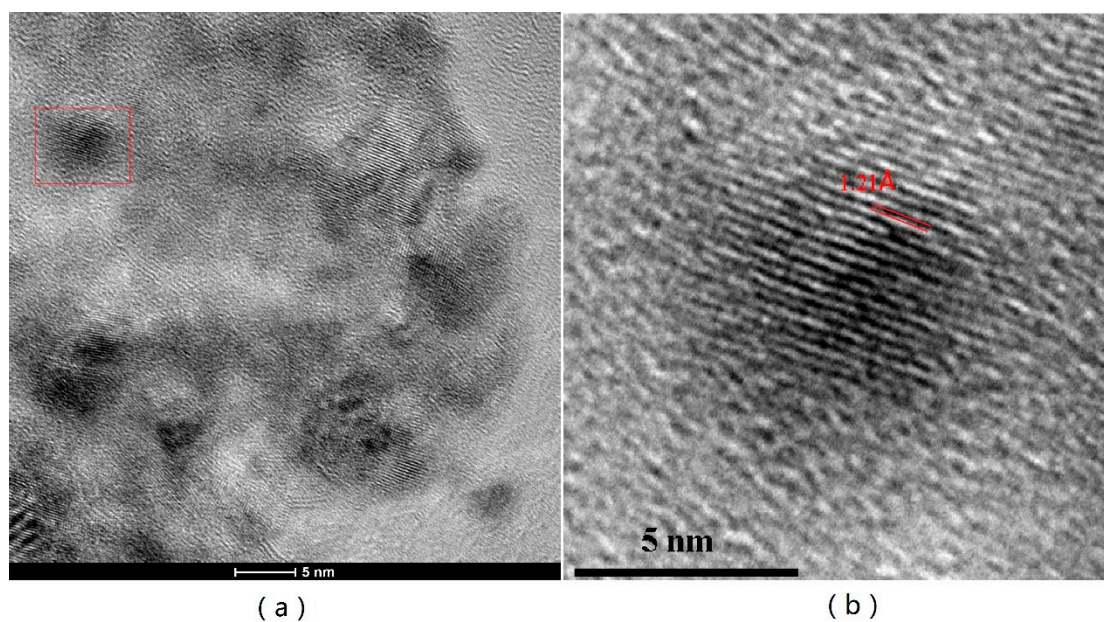


Figure 5. (a) High-Magnification Transmission Electron Microscope (HRTEM) of the CNMA-4 sample reduced with H_2 at $300\text{ }^\circ\text{C}$ for 2 h; (b) the image of HRTEM for a single particle from (a).

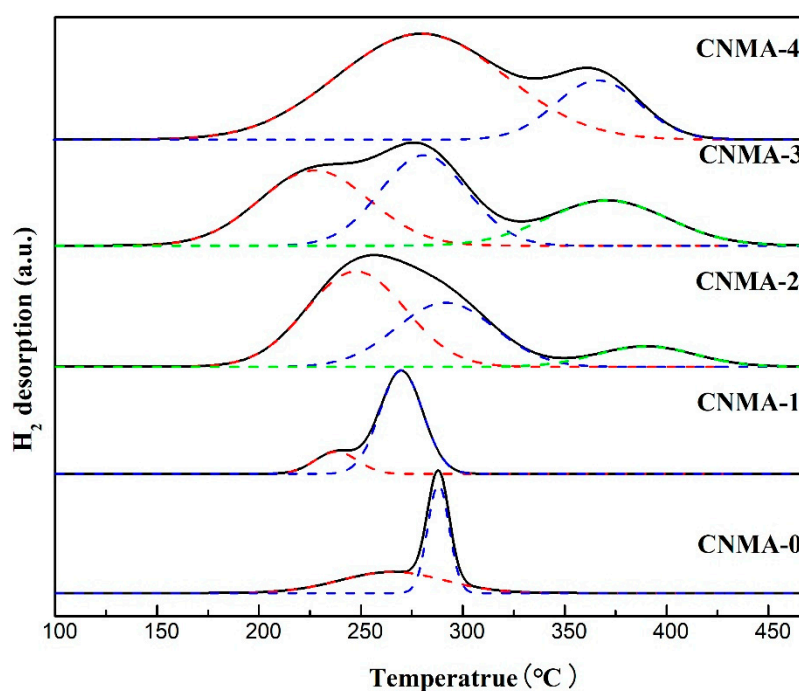


Figure 6. H_2 temperature-programmed reduction (H_2 -TPR) profiles of catalysts at $450\text{ }^\circ\text{C}$, the TPR, α , β , and γ peaks are shown as solid, dash dot, and dash and dot lines, respectively.

2.3. CO_2 -TPD

Figure 7 shows the CO_2 -TPD profiles for the reduced samples. The corresponding peak positions and contributions are listed in Table S4. The positions of desorption peaks range from 280 to $330\text{ }^\circ\text{C}$. The peak position at $240\text{ }^\circ\text{C}$ corresponds to the interaction of CO_2 with OH^- or O atoms. The medium-strength site (above $300\text{ }^\circ\text{C}$), was mainly attributed to Mg–O, Ni–O and Al–O. It can be found that CNMA-0 has the minimum number of strong basic sites among these samples as a result of

no Ni introduction. It is worth noting that the addition of Ni promoted the CO₂ adsorption on the catalyst surface due to the increase of total basicity of catalysts. This trend is similar to the results reported by Debek et al. [35]. CNMA-4 has the maximum number of strongly basic sites of these catalysts, possibly due to the introduction of Ni, increasing the Ni–O pair. In addition, the decrease in Cu content could result in the increase of basic sites. Marcu et al. also reported that the strong and total basic sites of Cu-based catalysts increase with the decline of the copper content [36].

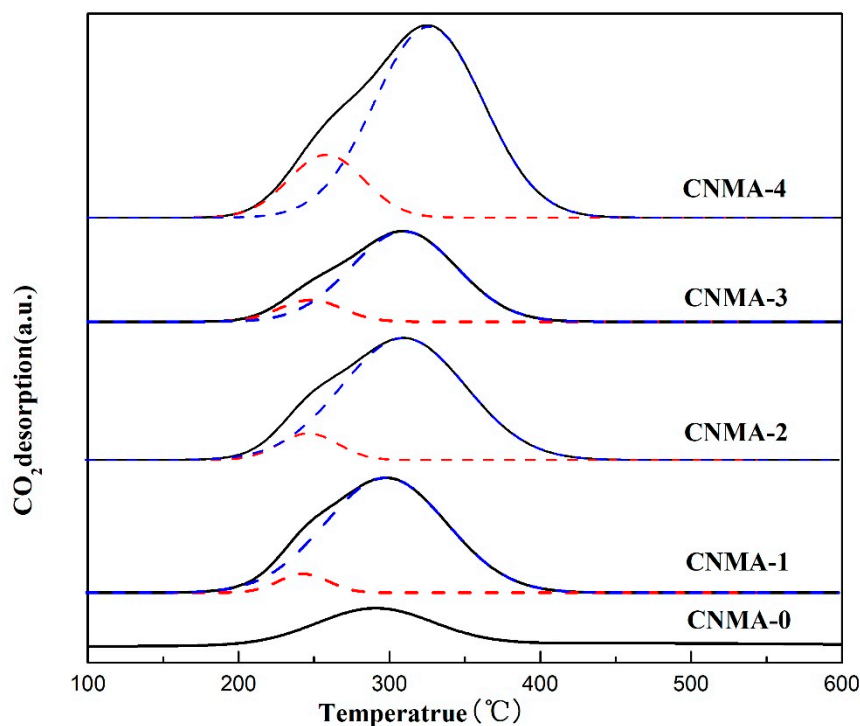


Figure 7. CO₂ temperature desorption spectroscopy (CO₂-TPD) profiles of the reduced samples with different Ni amounts, the TPD, α and β peaks are shown as solid, dash and dot lines, respectively.

2.4. Catalytic Performance

The activity and selectivity of the samples were examined through the conversion of CHCH to OPP. Figure 8 shows the relationship between the selectivity, conversion, and atomic ratios of Cu²⁺/Ni²⁺ after the catalytic reaction for 5 h. The catalysts with different Ni content exhibited different catalytic performances. The conversion of CHCH was over 95% after 5 h for CNMA-0 to CNMA-4, moreover, the conversion percentage increased with an increasing proportion of Ni in the samples. CNMA-1 and CNMA-2 showed higher selectivity and the selectivity clearly declined at the beginning of reaction. The introduction of a small amount of Ni destroys the metal–O bond, thus reducing the stability of the catalyst. The OPP selectivity of all the catalysts declined continuously with time of reaction. CNMA-4 still maintained a high selectivity for OPP after 5 h of reaction. This result can be attributed to higher BET surface areas and a smaller size of copper particles for CNMA-4. Based on the TEM images of the samples, a slightly smaller mean size of Cu⁰ particles was observed for CNMA-4 (3.82 nm) compared to CNMA-0 (5.20 nm). In addition, the precursor for CNMA-4 had better crystallinity and thin ordered laminates due to the presence of Ni (as confirmed by SEM), which lead to higher specific surface area and larger pore volume. The thin ordered structure can be ascribed to the substitution of Cu²⁺ by Ni²⁺ in the hydroxalcite laminates. This substitution results in a thinner layer structure due to the small ionic size of Ni²⁺ (0.069 nm for Ni²⁺ and 0.073 nm for Cu²⁺ in an octahedral coordination) [37]. The CNMA-4 sample has the highest specific surface area, better dispersion of CuO, and much stronger basic sites. The initial stage of CHCH dehydrogenation

may have occurred via H^+ abstraction on the basic sites [38]. Zeng et al. found that the distribution of alkaline sites and Cu species on the Cu-based catalytic surface has a strong effect on the selectivity of OPP, the strong basic sites may weaken the interaction of Al_2O_3 and CuO, preventing the active sites from undergoing agglomeration [3]. Wang et al. also reported that better dispersion of CuO in catalysts has a significant impact on the catalytic activity [39]. According to the TPR results, it is clear that CNMA-4 exhibits the highest ratio of low temperature peak (above 77.60%), which can be ascribed to the well dispersed copper species in CNMA-4.

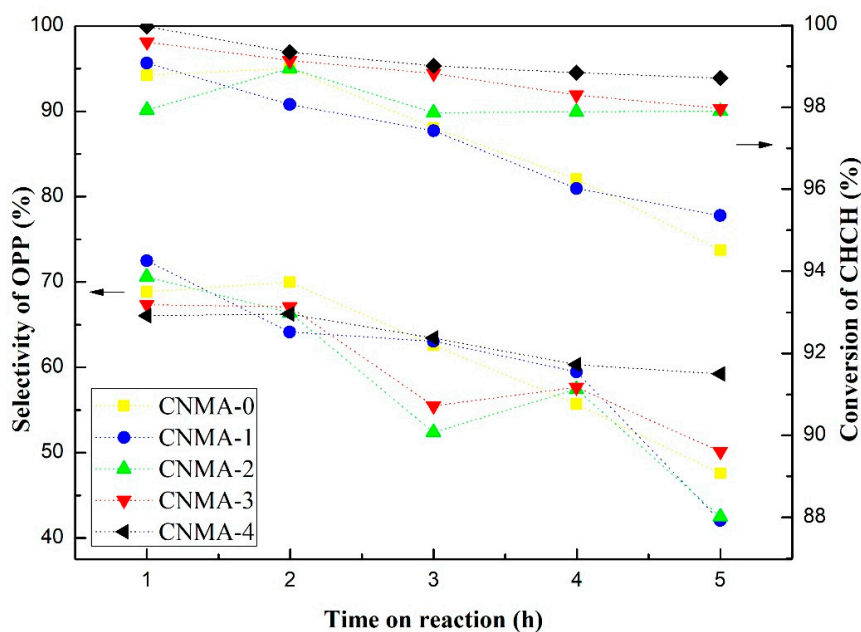


Figure 8. The stability of catalysts with different Ni content at 330 °C. (OPP: O-phenylphenol, CHCH: 2-(1-cyclohexenyl) cyclohexanone).

In order to clarify the impact of the content of Ni on the distribution of products, Figure 9 shows the relationship between the catalytic selectivity of catalysts and the primary products after a reaction time of 5 h. In our previous work, we have reported the catalytic mechanism and process of a Cu-based catalyst for the conversion of CHCH to OPP; O-cyclohexylcyclohexanone (OCC) and o-cyclohexylphenol (OCHP) were the main byproducts. In addition, a small amount of dibenzofuran (DBF) and biphenyl (BP) formed due to the further reaction of OPP [3,40]. OCC is the product of the hydrogenation of CHCH. Meanwhile, OCHP could also be generated by the dehydrogenation of OCC. OCHP was further dehydrogenated to form OPP. The selectivity of OPP is significantly affected by the content of Ni. With an increase in the content of Ni, the proportions of OCC and OCHP in the products decline greatly, while that of OPP increases. CNMA-4 showed the highest selectivity and lower proportion of byproducts after a reaction time of 5 h. These results can be attributed to a strongly basic site, higher BET surface area, and high Cu dispersion of CNMA-4. It is clear that the introduction of Ni can help enhance the selectivity of OPP, while inhibiting the formation of OCC and OCHP.

To further assess the stability of CNMA-4, Figure 10 shows the selectivity of OPP on CNMA-4 after a reaction time of 20 h. It can be seen that the selectivity of OPP declined by approximately 25%. As the yield of OPP declines, the yield of OCC increases; the yield of OCHP increases slowly as the reaction progresses. This indicates that the conversion to OCC in this reaction is a main factor, which resulted in the decrease of selectivity of OPP, perhaps due to the agglomeration of copper particles at high temperature. The Cu^0 particle size of catalysts increased at high temperatures and resulted in a worse dispersion and lower catalytic activity [40,41]. Similar observations were also reported on the agglomeration of MgO at high temperature by Auer et al. [42]. The low dispersibility of MgO weakens

the interaction between Cu and Mg, and further reduces the hydrogenation and dehydrogenation activity of the catalysts. Thus, the amount of byproducts OCC and OCHP increases. The improvement on the dehydrogenation performance of the catalyst will be the focus of our future research.

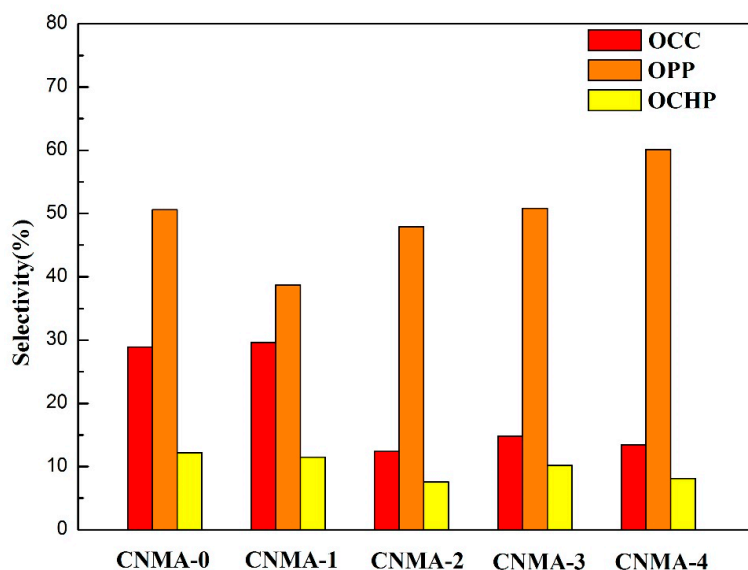


Figure 9. The selectivity for three types of main products for all samples after a reaction time of 5 h. (OPP: O-phenylphenol, OCC: O-cyclohexylcyclohexanone, OCHP: O-cyclohexylphenol).

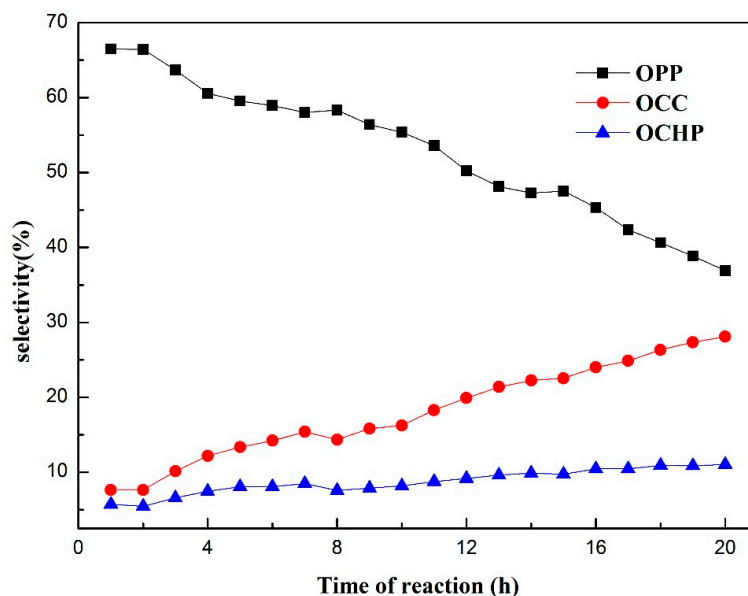


Figure 10. Stability test on CNMA-4 at 330 °C for 20 h.

3. Experimental

3.1. Preparation of Samples

In this work, LDH precursors were synthesized by co-precipitation, the molar ratio of $(\text{Cu}^{2+} + \text{Ni}^{2+})/\text{Mg}^{2+}/\text{Al}^{3+} = 2.5:3.5:2$, and the ratio of $\text{Ni}^{2+}/(\text{Cu}^{2+} + \text{Ni}^{2+})$ was changed from 0 to 0.4. The Cu:Ni:Mg:Al molar ratios of the five precursor samples were 2.5:0:3.5:2, 2.25:0.25:3.5:2, 2:0.5:3.5:2, 1.75:0.75:3.5:2, and 1.5:1:3.5:2, which were denoted by CNMA-0, CNMA-1, CNMA-2, CNMA-3, and CNMA-4, respectively. Solution A was prepared with mixed nitrates of Cu^{2+} , Ni^{2+} , Mg^{2+} , and Al^{3+}

dissolved in a certain amount of deionized water. The total concentration of metal ions ($\text{Cu}^{2+} + \text{Ni}^{2+} + \text{Mg}^{2+} + \text{Al}^{3+}$) in solution A was 0.9 mol/L. Solution A and a mixed solution B, with 1.00 mol/L Na_2CO_3 and NaOH, were added into the flask at 3 mL/min with stirring; pH was maintained at 9.5 and the solution was heated to 60 °C. The mixture was stirred for 6 h at 60 °C. After cooling and filtration, the product was washed with deionized water until pH = 7. The washed products were dried at 100 °C for 12 h and calcined at 450 °C for 4 h. The calcined samples were extruded through a molding device into a columnar shape to obtain the composite metal oxide catalyst ($\text{Ø}2 \times 0$ mm). The catalyst was obtained with hydrogen reduction ($20 \text{ mL}\cdot\text{min}^{-1}$) at 300 °C for 2 h.

3.2. Sample Characterization

XRD (X-ray diffraction) patterns were obtained from a X-ray diffractometer (Bruker AXS, D8 Advance, Karlsruhe, BW, Germany) with Cu $K\alpha$ radiation ($\lambda = 1.5406 \text{ \AA}$). The intensity data step was 0.05° in the 2θ range of $5\text{--}70^\circ$ and the counting time for each point at 40 kV and 40 mA was 1 s. FT-IR spectra were obtained with the KBr pellet technique in the range of $4000\text{--}400 \text{ cm}^{-1}$ on a Bruker Tensor 27 Fourier transforms spectrometer (Bruker AXS, Karlsruhe, BW, Germany). SEM (Scanning Electron Microscope) was performed on a Hitachi, S-4800II (Hitachi, Tokyo, Japan). The sample was evenly applied to the surface of the solid conductive adhesive, the surface of the sample was treated with gold, and then the sample was placed in the instrument to observe the sample morphology. Thermogravimetric analysis (TG-DTG) was conducted using a PerkinElmer TGA 1 from room temperature to 700 °C with a heating rate of $10 \text{ }^\circ\text{C}\cdot\text{min}^{-1}$ under N_2 . TEM (Transmission electron microscope) was performed using a Philips Tecnai 12 electron microscope (Philips, Amsterdam, NH, Holland). The hydrotalcite-like precursors were suspended in a solution of ethanol and then deposited over a carbon-coated copper grid, followed by solvent evaporation in air at room temperature. High-Magnification Transmission Electron Microscope (HRTEM) photographs were taken using Tecnai G2 F30 S-TWIN equipment (FEI, Hillsboro, OR, USA). N_2 adsorption isotherms of the samples were measured on Sorptomatic 1990 (Thermo Electron Co, Waltham, MA, USA). The sample surface area and pore volume were determined from the BET equation and Barrett–Joyner–Hallender (BJH) methods, respectively. The samples were outgassed at 200 °C under vacuum for 6 h prior to measurement. H_2 temperature-programmed reduction (H_2 -TPR) data were collected on a Finesorb-3010 (Finetec Instruments, Hangzhou, China). The sample was treated with pure Ar ($30 \text{ mL}\cdot\text{min}^{-1}$) up to 200 °C ($10 \text{ }^\circ\text{C}\cdot\text{min}^{-1}$) and maintained at this temperature for 30 min. After cooling to 100 °C, the samples for the TPR experiment, in a H_2/Ar mixture (1:9, $30 \text{ mL}\cdot\text{min}^{-1}$), were heated to 500 °C. Then the catalyst bed was flushed with Ar and cooled to room temperature. CO_2 temperature desorption spectroscopy (CO_2 -TPD) experiments were performed using a Finesorb-3010 chemical adsorption instrument loaded with 0.1 g of the catalyst. The catalyst was first treated for 30 min at 200 °C ($10 \text{ }^\circ\text{C}\cdot\text{min}^{-1}$), and then cooled to 100 °C. The sample was then flushed with CO_2 ($30 \text{ mL}\cdot\text{min}^{-1}$) for 1 h. Subsequently, the catalyst was flushed with Ar ($30 \text{ mL}\cdot\text{min}^{-1}$) for 30 min. Finally, the samples for CO_2 -TPD were heated to 600 °C at a rate of $10 \text{ }^\circ\text{C}\cdot\text{min}^{-1}$ in the presence of pure Ar at a rate of $30 \text{ mL}\cdot\text{min}^{-1}$. The catalysts were then cooled to 20 °C with pure Ar.

3.3. Catalytic Performance Test

The CHCH dehydrogenation and hydrogenation reaction was performed in a fixed-bed reactor. The whole apparatus consisted of five parts, including the temperature controller, feeding part, vapor generator, cooling section, and quartz reaction tube. Three grams of catalyst was placed in the middle of the tube and both sides of the tube were filled with glass beads with a diameter of 2–3 mm. The catalyst was reduced with hydrogen ($20 \text{ mL}\cdot\text{min}^{-1}$) at 300 °C for 2 h. The reaction was performed at 330 °C under atmospheric pressure. We adjusted the flow rate of H_2 to $20 \text{ mL}\cdot\text{min}^{-1}$ and used an injection pump [liquid hour space velocity (LHSV) = 0.2 h^{-1}] to add the reagent into the reactor. The product was dissolved in 3 mL of ethanol and measured by a chromatograph equipped with a flame ionization detector (FID) detector.

4. Conclusions

Hydrotalcite-like precursors with different $\text{Ni}^{2+}/(\text{Ni}^{2+} + \text{Cu}^{2+})$ atomic ratios were successfully prepared via the coprecipitation method. The introduction of Ni does not destroy the hydrotalcite-like structure. However, it reduces the thickness of the hydrotalcite laminates. The activity and stability of the catalysts are related to the content of Ni. The smaller sized Cu particles of CNMA-1 and CNMA-2 resulted in better initial catalytic selectivity. The introduction of Ni can improve the dispersibility of Cu^0 particles in catalysts and create strongly basic sites. CNMA-4 showed optimal stability and high selectivity around 60% after a reaction time of 5 h.

Supplementary Materials: The following are available online at <http://www.mdpi.com/2073-4344/8/5/186/s1>, Figure S1: FT-IR image of Cu/Ni/Mg/Al before calcination (a) and calcination (b), Figure S2: TG-DTG of the precursors in N_2 , Figure S3: N_2 adsorption-desorption isotherms of CNMA-(0-4), Figure S4. The pore size distributions for all catalysts, Figure S5: HRTEM and elemental mapping images of catalysts after reduction (a) Cu/Mg/Al/Ni catalysts (b) Cu-K map (c) Ni-K map (d) Mg-K map (e) Al-K map, Table S1: FWHM and the size of Cu^0 particles by XRD, Table S2: The properties of the samples with different amount of Ni, Table S3: Temperatures for Reduction peak and the percentage of α peak for these samples, Table S4: Distribution of the basic type for the samples with different Ni amount.

Author Contributions: Y.Z. and T.Z. conceived and designed the experiments; J.W. and T.Z. performed the experiments; Y.Z., J.W. and T.Z. analyzed the data. Y.Z., T.Z., J.W., K.L. and Y.C. wrote the paper.

Acknowledgments: Y.Z. acknowledges funding from the National Natural Science Foundation of China (Grant No. 21676231) and generous allocations of test provided by the testing Center of Yangzhou University and Scgrid plan of CAS. We thank the projects sponsored by the Priority Academic Program Development of Jiangsu Higher Education Institutions and Qing Lan of Yangzhou University.

Conflicts of Interest: The authors declare no conflicts of interest.

References

1. Hu, R.; Xiao, X.; Tu, S.; Zuo, X.; Nan, J. Synthesis of flower-like heterostructured $\beta\text{-Bi}_2\text{O}_3/\text{Bi}_2\text{O}_2\text{CO}_3$ microspheres using $\text{Bi}_2\text{O}_2\text{CO}_3$ self-sacrifice precursor and its visible-light-induced photocatalytic degradation of o-phenylphenol. *Appl. Catal. B Environ.* **2015**, *163*, 510–519. [[CrossRef](#)]
2. Bomhard, E.M.; Brendler-Schwaab, S.Y.; Freyberger, A.; Herbold, B.A.; Leser, K.H.; Richter, M. O-phenylphenol and its sodium and potassium salts: A toxicological assessment. *Crit. Rev. Toxicol.* **2002**, *32*, 551–626. [[CrossRef](#)] [[PubMed](#)]
3. Zeng, Y.; Zhang, T.; Xu, Y.; Ye, T.; Wang, R.; Yang, Z.; Jia, Z.; Ju, S. Cu/mg/al hydrotalcite-like hydroxide catalysts for o-phenylphenol synthesis. *Appl. Clay. Sci.* **2016**, *126*, 207–214. [[CrossRef](#)]
4. Goto, H.; Shibamoto, N.; Tanaka, S. Process for Preparing O-Phenylphenol. U.S. Patents 4088702, 29 November 1977.
5. Imafuku, K.; Oda, J.; Itoh, K.; Matsumura, H. Dehydrogenation of 2-(1-cyclohexenyl) cyclohexanone with palladium catalyst. *Bull. Chem. Soc. Jpn.* **1974**, *47*, 1201–1202. [[CrossRef](#)]
6. Matsumura, H.; Imafuku, K.; Takano, I.; Matsuura, S. Rearrangements in the palladium-catalyzed dehydrogenation of cyclohexylphenols to phenylphenols. *Bull. Chem. Soc. Jpn.* **1971**, *44*, 567. [[CrossRef](#)]
7. Jin, D.; Zhu, B.; Hou, Z.; Fei, J.; Lou, H.; Zheng, X. Dimethyl ether synthesis via methanol and syngas over rare earth metals modified zeolite y and dual Cu-Mn-Zn catalysts. *Fuel* **2007**, *86*, 2707–2713. [[CrossRef](#)]
8. Cavani, F.; Trifirò, F.; Vaccari, A. Hydrotalcite-type anionic clays: Preparation, properties and applications. *Catal. Today* **1991**, *11*, 173–301. [[CrossRef](#)]
9. Zhang, Y.-S.; Li, C.; Yu, C.; Tran, T.; Guo, F.; Yang, Y.; Yu, J.; Xu, G. Synthesis, characterization and activity evaluation of Cu-based catalysts derived from layered double hydroxides (ldhs) for denox reaction. *Chem. Eng. J.* **2017**, *330*, 1082–1090. [[CrossRef](#)]
10. Patankar, S.C.; Yadav, G.D. Cascade engineered synthesis of 2-ethyl-1-hexanol from n-butanal and 2-methyl-1-pentanol from n-propanal using combustion synthesized Cu/Mg/Al mixed metal oxide trifunctional catalyst. *Catal. Today* **2017**, *291*, 223–233. [[CrossRef](#)]
11. Jiang, Z.; Kong, L.; Chu, Z.; France, L.J.; Xiao, T.; Edwards, P.P. Catalytic combustion of propane over mixed oxides derived from $\text{Cu}_x\text{Mg}_{3-x}\text{Al}$ hydrotalcites. *Fuel* **2012**, *96*, 257–263. [[CrossRef](#)]

12. Zhou, C.-H.; Beltramini, J.N.; Lin, C.-X.; Xu, Z.-P.; Lu, G.Q.; Tanksale, A. Selective oxidation of biorenewable glycerol with molecular oxygen over Cu-containing layered double hydroxide-based catalysts. *Catal. Sci. Technol.* **2011**, *1*, 111–122. [[CrossRef](#)]
13. Shi, G.; Jin, K.; Su, L.; Shen, J. Synthesis of Ni/SiO₂ catalysts and their performances in glycerol hydrogenolysis to 1,2-propanediol. *J. Mol. Catal.* **2015**, *29*, 403–413.
14. Shi, G.; Su, L.; Jin, K. New bulk nickel phosphide catalysts for glycerol hydrogenolysis to 1,2-propanediol. *Catal. Commun.* **2015**, *59*, 180–183. [[CrossRef](#)]
15. Alejandre, A.; Medina, F.; Rodriguez, X.; Salagre, P.; Cesteros, Y.; Sueiras, J.E. Cu/Ni/Al layered double hydroxides as precursors of catalysts for the wet air oxidation of phenol aqueous solutions. *Appl. Catal. B Environ.* **2001**, *30*, 195–207. [[CrossRef](#)]
16. Marino, F.; Baronetti, G.; Jobbagy, M.; Laborde, M. Cu-ni-k/gamma-al2o3 supported catalysts for ethanol steam reforming formation of hydrotalcite-type compounds as a result of metal-support interaction. *Appl. Catal. A Gen.* **2003**, *238*, 41–54. [[CrossRef](#)]
17. Mott, D.; Galkowski, J.; Wang, L.; Luo, J.; Zhong, C.-J. Synthesis of size-controlled and shaped copper nanoparticles. *Langmuir* **2007**, *23*, 5740–5745. [[CrossRef](#)] [[PubMed](#)]
18. Reichle, W.T.; Kang, S.Y.; Everhardt, D.S. The nature of the thermal decomposition of a catalytically active anionic clay mineral. *J. Catal.* **1986**, *101*, 352–359. [[CrossRef](#)]
19. Kannan, S.; Dubey, A.; Knozinger, H. Synthesis and characterization of cumgal ternary hydrotalcites as catalysts for the hydroxylation of phenol. *J. Catal.* **2005**, *231*, 381–392. [[CrossRef](#)]
20. Zhu, K.; Liu, C.; Ye, X.; Wu, Y. Catalysis of hydrotalcite-like compounds in liquid phase oxidation: (i) phenol hydroxylation. *Appl. Catal. A Gen.* **1998**, *168*, 365–372. [[CrossRef](#)]
21. Dubey, A.; Kannan, S.; Velu, S.; Suzuki, K. Catalytic hydroxylation of phenol over CuM(II)M(III) ternary hydrotalcites, where M(II) = Ni or Co and M(III) = Al, Cr or Fe. *Appl. Catal. A Gen.* **2003**, *238*, 319–326. [[CrossRef](#)]
22. Takehira, K.; Shishido, T.; Wang, P.; Kosaka, T.; Takaki, K. Autothermal reforming of CH₄ over supported Ni catalysts prepared from Mg-Al hydrotalcite-like anionic clay. *J. Catal.* **2004**, *221*, 43–54. [[CrossRef](#)]
23. De Bokx, P.; Wassenberg, W.; Geus, J. Interaction of nickel ions with a γ -Al₂O₃ support during deposition from aqueous solution. *J. Catal.* **1987**, *104*, 86–98. [[CrossRef](#)]
24. Ni, Z.; Chen, A.; Fang, C.; Wang, L.; Yu, W. Enhanced nox adsorption using calcined Zn/Mg/Ni/Al hydrotalcite-like compounds. *J. Phys. Chem. Solids* **2009**, *70*, 632–638. [[CrossRef](#)]
25. Costantino, U.; Curini, M.; Montanari, F.; Nocchetti, M.; Rosati, O. Hydrotalcite-like compounds as catalysts in liquid phase organic synthesis: I. Knoevenagel condensation promoted by [Ni_{0.73}Al_{0.27}(OH)₂](CO₃)_{0.135}. *J. Mol. Catal. A Chem.* **2003**, *195*, 245–252. [[CrossRef](#)]
26. Jitianu, M.; Bălăsoiu, M.; Marchidan, R.; Zaharescu, M.; Crisan, D.; Craiu, M. Thermal behaviour of hydrotalcite-like compounds: Study of the resulting oxidic forms. *Int. J. Inorg. Mater.* **2000**, *2*, 287–300. [[CrossRef](#)]
27. Busca, G.; Lorenzelli, V. Infrared spectroscopic identification of species arising from reactive adsorption of carbon oxides on metal oxide surfaces. *Mater. Chem.* **1982**, *7*, 89–126. [[CrossRef](#)]
28. Anillo, A.A.; Villa-García, M.A.A.; Llavona, R.; Suárez, M.; Rodríguez, J. Textural properties of α -titanium(iv) phenylphosphonate: Influence of preparation conditions. *Mater. Res. Bull.* **1999**, *34*, 627–640. [[CrossRef](#)]
29. Kubiak, G.D.; Sitz, G.O.; Zare, R.N. Recombinative desorption dynamics: Molecular hydrogen from Cu(110) and Cu(111). *J. Chem. Phys.* **1985**, *83*, 2538–2551. [[CrossRef](#)]
30. Guo, X.; Mao, D.; Lu, G.; Wang, S.; Wu, G. Glycine-nitrate combustion synthesis of CuO-ZnO-ZrO₂ catalysts for methanol synthesis from CO₂ hydrogenation. *J. Catal.* **2010**, *271*, 178–185. [[CrossRef](#)]
31. Li, D.; Koike, M.; Chen, J.; Nakagawa, Y.; Tomishige, K. Preparation of Ni-Cu/Mg/Al catalysts from hydrotalcite-like compounds for hydrogen production by steam reforming of biomass tar. *Int. J. Hydrog. Energy* **2014**, *39*, 10959–10970. [[CrossRef](#)]
32. Rynkowski, J.M.; Paryjczak, T.; Lenik, M. On the nature of oxidic nickel phases in NiO/ γ -Al₂O₃ catalysts. *Appl. Catal. A Gen.* **1993**, *106*, 73–82. [[CrossRef](#)]
33. Flores, J.H.; Peixoto, D.P.B.; Appel, L.G.; de Avillez, R.R.; Silva, M.I.P.D. The influence of different methanol synthesis catalysts on direct synthesis of dme from syngas. *Catal. Today* **2011**, *172*, 218–225. [[CrossRef](#)]
34. Shi, G.; Fang, D.; Shen, J. Hydroisomerization of model FCC naphtha over sulfided Co(Ni)-Mo(W)/MCM-41 catalysts. *Mesoporous. Mater.* **2009**, *120*, 339–345. [[CrossRef](#)]

35. Dębek, R.; Radlik, M.; Motak, M.; Galvez, M.E.; Turek, W.; Da Costa, P.; Grzybek, T. Ni-containing Ce-promoted hydrotalcite derived materials as catalysts for methane reforming with carbon dioxide at low temperature—On the effect of basicity. *Catal. Today* **2015**, *257*, 59–65. [[CrossRef](#)]
36. Marcu, I.-C.; Tichit, D.; Fajula, F.; Tanchoux, N. Catalytic valorization of bioethanol over Cu-Mg-Al mixed oxide catalysts. *Catal. Today* **2009**, *147*, 231–238. [[CrossRef](#)]
37. Shannon, R. Revised effective ionic radii and systematic studies of interatomic distances in halides and chalcogenides. *Acta Crystallogr. Sect. A* **1976**, *32*, 751–767. [[CrossRef](#)]
38. Balasamy, R.J.; Tope, B.B.; Khurshid, A.; Al-Ali, A.A.S.; Atanda, L.A.; Sagata, K.; Asamoto, M.; Yahiro, H.; Nomura, K.; Sano, T.; et al. Ethylbenzene dehydrogenation over FeO_x/(Mg,Zn)(Al)O catalysts derived from hydrotalcites: Role of MgO as basic sites. *Appl. Catal. A Gen.* **2011**, *398*, 113–122. [[CrossRef](#)]
39. Wang, L.-C.; Liu, Q.; Chen, M.; Liu, Y.-M.; Cao, Y.; Fan, K.-N. Structural evolution and catalytic properties of nanostructured Cu/ZrO₂ catalysts prepared by oxalate gel-coprecipitation technique. *J. Phys. Chem. C* **2007**, *111*, 16549–16557. [[CrossRef](#)]
40. Zeng, Y.; Zhang, T.; Xu, Y.; Hu, P.; Ye, T.; Jia, Z.; Ju, S. Cu/Mg/Al/Zr non-noble metal catalysts for o-phenylphenol synthesis. *RSC Adv.* **2016**, *6*, 6737–6746. [[CrossRef](#)]
41. Jiang, Z.; Hao, Z.; Yu, J.; Hou, H.; Hu, C.; Su, J. Catalytic combustion of methane on novel catalysts derived from Cu-Mg/Al-hydrotalcites. *Catal. Lett.* **2005**, *99*, 157–163. [[CrossRef](#)]
42. Auer, S.M.; Gredig, S.V.; Köppel, R.A.; Baiker, A. Synthesis of methylamines from CO₂, H₂ and NH₃ over Cu-Mg-Al mixed oxides. *J. Mol. Catal. A Chem.* **1999**, *141*, 193–203. [[CrossRef](#)]



© 2018 by the authors. Licensee MDPI, Basel, Switzerland. This article is an open access article distributed under the terms and conditions of the Creative Commons Attribution (CC BY) license (<http://creativecommons.org/licenses/by/4.0/>).